ETH zürich

ETH Library

Macroporous Aligned Hydrogel Microstrands for 3D Cell Guidance

Journal Article

Author(s):
Rizzo, Riccardo; Bonato, Angela; Chansoria, Parth; Zenobi-Wong, Marcy

Publication date:
2022-09-12

Permanent link:
https://doi.org/https://doi.org/10.3929/ethz-b-000564954

Rights / license:
Creative Commons Attribution 4.0 International

Originally published in:
ACS Biomaterials Science & Engineering 8(9), https://doi.org/10.1021/acsbiomaterials.2c00370

This page was generated automatically upon download from the ETH Zurich Research Collection.
For more information, please consult the Terms of use.

Macroporous Aligned Hydrogel Microstrands for 3D Cell Guidance

Riccardo Rizzo[a,‡], *Angela Bonato*[a, ‡], *Parth Chansoria*[a], *Marcy Zenobi-Wong*[a,*]

‡These authors contributed equally.

[a]Tissue Engineering + Biofabrication Laboratory, Department of Health Sciences and Technology, ETH Zürich, Otto-Stern-Weg 7, Zürich, 8093 Switzerland

Keywords: alignment, microstrand, macroporosity, muscle tissue engineering, norbornene, photoclick

Abstract. Tissue engineering strongly relies on the use of hydrogels as highly hydrated 3D matrices to support the maturation of laden cells. However, due to lack of microarchitecture and sufficient porosity, common hydrogel systems do not provide physical cell-instructive guidance cues and efficient transport of nutrients and oxygen to the inner part of the construct. A controlled, organized cellular alignment and resulting alignment of secreted ECM are hallmarks of muscle, tendons and nerves and play an important role in determining their functional properties. Although several strategies to induce cellular alignment have been investigated in 2D systems, the generation of cell-instructive 3D hydrogels remains a challenge. Here we report on the development of a simple and scalable method to efficiently generate highly macroporous constructs featuring aligned guidance cues. A pre-crosslinked bulk hydrogel is pressed thorough a grid with variable opening sizes, thus deconstructing it into an array of aligned, high aspect-

ratio microgels (microstrands) with tunable diameter, which are eventually stabilized by a second photo-click crosslinking step. This method has been investigated and optimized both *in silico* and *in vitro*, leading to conditions with excellent viability and organized cellular alignment. Finally, as proof of concept, the method has been shown to direct aligned muscle tissue maturation. These findings demonstrate the 3D physical guidance potential of our system which can be used for a variety of anisotropic tissues and applications.

1. Introduction

In the last decades hydrogels have been extensively employed in the field of tissue engineering and bioprinting due to their high hydration, cell support in a 3D environment, and bio-mimetic properties.[1-4] Although hydrogel-based bioprinting made it possible to generate complex macroscopic 3D shapes, the substantial homogeneity of common hydrogel formulations on a cellular scale lacks microstructure and porosity, both pivotal elements to guide tissue formation.[5-7] To direct tissue development and cell spatial arrangement within 3D matrices, the field has exploited two main approaches, namely the introduction of either biochemical or physical cues.

Biochemical cues such as adhesion peptides, small molecules, and growth factors have been bound to hydrogel-forming polymers in various ways and used extensively to enhance the bioactivity and cell-interactive properties of hydrogel systems.[8-10] They are reported to influence cell attachment, proliferation, and differentiation into the desired tissue type.[11] In the past twenty years, the study of the effect of bioactive signals on cell fate and behavior in 3D matrices has also been made possible with fine spatiotemporal control using sophisticated light-based techniques such as two-photon patterning.[12-16] Growth factors and small molecules have proved extremely valuable, since they can recapitulate the biosignalling milieu of the developing tissue

and act directly on cell migration, proliferation, and tissue maturation.[17-19] For example, adhesion peptides such as Arg-Gly-Asp (RGD) are widely used to mimic the presence of the extracellular matrix, thus favouring integrin-mediated cell adhesion.[10, 20] Although some bio-inert polymers need the incorporation of such small molecules to create anchor points for cells to better spread and migrate, other natural-derived polymers such as collagens or gelatin already possess such adhesion cues.[21-23]

Structural guidance of cells by physical cues is another powerful approach to directing tissue assembly and maturation.[24-26] Unlike biochemical cues, biophysical ones persist for longer and are more versatile, as their stiffness, porosity, pore size, structural anisotropy can all be controlled.[11] Polymer concentration and degree of substitution influence the resulting hydrogel stiffness, which has been shown to strongly influence stem cell fate towards differentiation into distinct tissues.[27-29] Porosity of the matrix is another important physical cue. It improves cell infiltration and migration, while also facilitating the diffusion of nutrients in the inner part of the construct in the absence of vascularization.[6] Several methods for producing porous hydrogel systems have been investigated, such as phase-transition,[30] freeze-drying,[31] use of microribbons[32-33] or sacrificial porogens,[34-35] to name a few, and more recently the deconstruction of preformed hydrogels via sizing through a grid.[36] Although some manufacturing techniques ensure size-controlled, macroporous and biocompatible hydrogels, they often lack defined pore orientation and interconnection throughout the construct. Generation of complex, anisotropic cellular organization, such as the one found in vasculature or musculoskeletal and connective tissues, plays a critical role in tissue microarchitecture, impacting both biological and mechanical properties of the tissue; it relies on geometrical constraints that can induce directional cell orientation.[37-38]

The above-mentioned desired characteristics for an engineered construct for controlling cell behavior eventually need to also meet a size requirement for the intended application (i.e., *in vitro* model, *in vivo* implantation). Commonly, fabrication methods that are precise at a small scale also require lengthy processing times that pose a major limitation on cell viability. On the other hand, quick and easy manufacturing techniques of large constructs may be less damaging to the cells but then lack the microstructure and macroporosity needed to instruct cell architecture at the microscopic level.

Here, we report on the development of a simple and scalable method to produce anisotropic macroporous constructs with high aspect ratio-aligned microgels (microstrands) acting as physical guidance cues. By pressing a gelatin-based bulk hydrogel through a grid with tunable opening size, aligned microstrands are generated. The sized constructs are then stabilized for cell culture by a secondary crosslinking step based on state-of-the-art photoclick thiol-norbornene reaction. Encapsulated cells benefit from oriented macroporosity that permits nutrient and oxygen supply within the construct and from the aligned microstrands providing a preferred direction of growth. The sizing method is simple, fast, easily upscalable, and it can be carried out without special expertise, thus making it an attractive solution for the generation of various aligned tissue formations. In this work, we adopted myoblasts as a proof-of-concept model for aligned muscle tissue development.

2. Materials and Methods

Unless indicated otherwise all chemicals are purchased from Merck and cell culture reagents from Gibco.

Synthesis of Gelatin Norbornene (Gel-NB)

Synthesis protocol was adapted from Rizzo et al. (Figure S1A).[39] In short, 50 g of gelatin type A from porcine skin were first dissolved in pH 9 0.1 M carbonate-bicarbonate buffer at 10% at 50°C. When completely dissolved, 1 g of cis-5-norbornene-endo-2,3-dicarboxylic anhydride (CA) was added to the reaction mixture under vigorous stirring. After 10 minutes the pH was checked and adjusted to 9 using NaOH 1M before the addition of another gram of norbornene reactant. The same procedure was repeated up to the addition of a total of 5 g of CA. 20 minutes after the last addition, the solution was diluted two-fold in pre-warmed mQ H2O and the pH adjusted to 7 with the addition of HCl 1 M. The solution was then centrifuged for 15 min at 3000 rcf and the supernatant dialysed for 3-4 days against mQ H2O at 40°C with frequent water changes and finally freeze-dried. Gel-NB degree of substitution (DS) was calculated using ^{1}H-NMR (Bruker Ultrashield 400 MHz, 1024 scans), as previously reported (n = 3, see Figure S2, Supporting Information).[39]

Synthesis of Gelatin Thiol (Gel-SH)

Gelatin type A from porcine skin (25 g) was dissolved in 1.25 L of pH 4 150 mM MES buffer warmed to 40°C for a final concentration of 2%. When completely dissolved, 2.38 g (10 mmol) of 3,3'-dithiobis(proprionohydrazide) (DTPHY) were added to the reaction mixture. Once completely dissolved, 3.83 g (20 mmol) of 1-ethyl-3-(3'-dimethylaminopropyl)carbodiimide hydrochloride (EDC) were added and the reaction was left to proceed at 40°C overnight. Then, tris(2-carboxyethyl)phosphine (8.6 g, 30 mmol) was added to the solution and the reduction of the disulfide bonds was left to proceed for 6 hours in sealed flask (Figure S1B). 1 g of NaCl was then added to the solution before dialysis against mQ H2O balanced to pH 4.5 with diluted HCl.

Finally, Gel-SH was freeze-dried and stored under inert atmosphere at –20°C prior to use. Gel-SH degree of substitution (DS) was determined by ^{1}H-NMR (Bruker Ultrashield 400 MHz, 1024 scans). In short, Gel-SH was solubilized in a solution of 3-(trimethylsilyl)-1-propanesulfonic acid (DSS) in D_2O (Apollo Scientific). DSS methyl protons (0.1 to – 0.1 ppm) were adopted as internal standards to calculate SH millimoles per gram of gelatin by comparison with DTPHY methylene protons (2.85 to 2.75 ppm and 2.7 to 2.6 ppm) (n = 3, see Figure S3, Supporting Information).

Sizing devices

The sizing devices used in this work were designed to fit inside a common 1 mL or 3 mL plastic syringe (Braun). These syringe holders were fabricated with a threaded end onto which a metal open cap was screwed to hold the desired grid in place (Figure 1A). The nylon grids had openings sizes of 20 µm, 40 µm, 100 µm (Merck Millipore) and 70 µm (cell strainer, Falcon). The grids were cut into 9, 13, or 18 mm diameter to fit into 1, 3, or 10 mL sizing devices, respectively. As illustrated in Figure 1A, the assembly of the sizing device consisted of positioning the cut nylon mesh into the open cap, which was then tightly screwed onto the metal syringe holder to secure enough tension on the nylon fibers to cut the hydrogel. For cell experiments, all the components were sterilized using 70% EtOH and UV treatment.

Sizing process: generation of aligned microstrands

Gel-SH and Gel-NB were mixed at SH:NB equimolar amount (1:1 ratio) in PBS at 37°C with a total polymer concentration (Gel-SH + Gel-NB) of 2%, 5%, or 10%. In each formulation, the photoinitiator lithium phenyl-2,4,6-trimethylbenzoylphosphinate (LAP) was used at 0.05%.

When completely solubilized, the photosensitive gelatin solution was filter-sterilized using 0.2 µm filters and then transferred to 1-mL or 3-mL sterile syringes, paying particular attention to avoid air bubbles. For the 10-mL sizing device, the solution was added directly into the stainless-steel tool previously sterilized with 70% EtOH and UV treatment. The syringes were then sealed with sterile plastic caps and parafilm, placed in ice, and protected from light. After 30 minutes on ice to allow for thermal crosslinking, the syringe tip was removed with a scalpel. The syringe filled with physically crosslinked photosensitive gelatin was then inserted into the sizing device, previously assembled as described above. By gently pushing on the syringe piston while moving it laterally, the hydrogel was sized onto a petri dish (see Video S1, Supporting Information). Following a 2-minute exposure in a UV box (405 nm) to covalently crosslink the aligned microstrands, the construct was cut into 1-cm pieces and transferred into cell culture media or PBS. UV intensity was found to be 6.6 mW/cm^2 using a Thorlabs power meter (PM100D equipped with S120VC Standard Photodiode Power Sensor). The video of the sizing process (Video S1 Supporting Information) and the pictures showing the system scalability (Figure 1B) were taken with a Fujifilm X-T3 camera.

Rheological analysis

Rheological measurements were carried out on an Anton Paar MCR 301 with 20 mm-parallel plate geometry. A wet tissue paper was added to the chamber to prevent Gel-NB/Gel-SH photoresins from drying during analysis. Storage and loss modulus of thermally crosslinked Gel-NB/Gel-SH formulations were obtained under oscillatory conditions (2 % strain, 1 Hz frequency, 0.2 mm gap, 10 seconds measuring point duration). The samples were first allowed to equilibrate at 37°C in the humidified chamber for 5 minutes prior to starting the measurements. Physical

crosslinking was induced with a linear cooling ramp (2 °C/min) from 37 °C to 8 °C (minimum temperature attainable) followed by 45 minutes at 8°C to reach plateau values. Following the oscillatory analysis, the samples were kept at 8°C to determine the yield stress by performing a strain sweep analysis with strain values going from 10^{-1} to 10^{3} (1 Hz frequency, 0.2 mm gap, 10 seconds measuring point duration). The yield stress was calculated as the peak value of the elastic stress (σ', product of storage modulus G' and strain amplitude) plotted against strain as previously reported.[40-41]

Initial viscosity and shear thinning behavior were characterized on thermoreversibly crosslinked photoresins in rotational tests (0.2 mm gap). The shear rate was increased logarithmically from 0.01 to 300 1/s, while the measurement point duration was decreased logarithmically from 300 s per point to 1 s per point.

Compression test of bulk hydrogels

TA.XTplus Texture Analyzer (Stable Micro Systems) equipped with a 500-g load cell was used to perform unconfined uniaxial compression tests. Solutions composed of 0.05% LAP and different total Gel-NB/Gel-SH concentrations (2%, 5%, 10%) in PBS were warmed to 37°C, filter sterilized and pipetted into PDMS molds of 4 mm in diameter and 2 mm in height. The samples were allowed to thermally crosslink in ice for 30 minutes, thus mimicking the temperature variation that occurs during the sizing procedure, and were then UV crosslinked for 2 minutes. After washing in PBS, the cylinders were placed between the compression plates and a 0.1-g pre-load was applied to ensure full contact. Samples were left to relax for 2 minutes and then compressed with a speed of 0.01 mm/s to 15% strain. The elastic compressive modulus was

determined by linear fitting of initial linear section of the stress-strain curve (0-5%). Measurements were performed in triplicates (n = 3).

SEM imaging

Aligned microstrands were prepared as indicated above. After washing in PBS, the crosslinked, structured hydrogels were cut into 1-2 mm slices with a scalpel and fixed in 4% paraformaldehyde in PBS for 2h at room temperature. Samples were then washed with Milli-Q H2O and dehydrated by stepwise treatment with ethanol in mQ H2O (30%, 50%, 70%, 90%, 100%), and then with hexamethyldisilazane (HMDS) in ethanol (30%, 50%, 70%, 90%, 100%) with a 20-minute incubation for each step. After 1 hour in 100% HDMS, samples were left to dry in a fume hood. Dried samples were sputter coated (CCU-010 HV, Safematic) with platinum-palladium (Pt/Pd) and imaged with a Hitachi SU5000 field emission SEM. Nylon grids were simply sputter coated with Pt/Pd prior to imaging.

Macroporosity and Percolation

Aligned microstrands were generated as described above using a total gelatin concentration of 2%. The aligned constructs were then submerged in a solution of high molecular weight FITC-Dextran (500 kDa) in PBS for 15 minutes. The percolation (fluid movement through porous material) of the fluorescent polymer in the macroporous construct was then imaged using a Leica SP8 confocal microscope (Leica) equipped with a 25x objective. Z-stacks of 100 µm were acquired from the sample surface with 1 µm z-steps. Images were processed using Fiji.

Computational modeling of the shear stress during sizing

The computational model constituted a steady-state inelastic non-Newtonian fluid flow model in COMSOL Multiphysics (COMSOL Inc, SE). The shear thinning characteristics of the photoresin at different concentrations (2, 5 and 10% w/v) was defined by the power-law:[42]

$$\mu(\gamma) = m\gamma^{n-1} \quad (1)$$

where μ is the dynamic viscosity of the resin, γ is the shear rate, and m and n are the flow consistency and flow behavior indices, respectively. Through rheological measurements of thermo-reversibly crosslinked photoresin samples at each concentration, the flow consistency indices were 22, 229, and 1750 Pa s for 2, 5, and 10% w/v resin concentration, respectively. Furthermore, a constant flow behavior index of 0.2 was deemed to generate the best-fit model for the dynamic viscosity variation with shear rate. The models comprising the sizing meshes constituted a small 3×3 grid of the sizing grid with a bulk fluid domain above the mesh (Figure 4B). The grid dimensions were determined from SEM images of the nylon meshes. A normal inflow velocity of 5 mm/s was applied at the fluid domain, mimicking the speed at which the sizing process was conducted, and a free-flow constraint was applied at the output of the sizing grid. A no-slip condition was applied at the walls of the sizing grid. As for the meshing criteria, a free tetrahedral mesh of maximum element size of 2 μm (i.e., one-tenth the size of the minimum feature dimension of 20 μm), similar to in previous studies, was applied.[43-44] A compilation time for a parametric sweep across the three flow consistency indices was 18 minutes. The resulting shear stress was plotted across the entire width of an opening within the sizing grid. For the model without the sizing grid, a simple cylindrical (Φ = 5 mm, h = 10 mm) shear thinning model was used and the shear stress determined throughout the entire width of the model.

Cell culture and encapsulation

C2C12 myoblasts were expanded in cell culture media composed of DMEM + 10% fetal bovine serum + 10 µg/mL gentamicin in 5-layer flasks (Falcon). C2C12 cells were trypsinized and mixed with warm (37°C) and sterile Gel-NB/Gel-SH photosensitive solutions at 10 million cells/mL. Following the sizing procedure described above, the cell-encapsulated aligned microstrands were directly transferred into 24-well plates and cultured from day 0 in differentiation media composed of DMEM + 2% horse serum + 1 % ITS (Corning) + 10 µg/mL gentamicin for up to 3 weeks with media change every other day. Videos of myotubes twitching (Video S2, Supplementary Information) were taken after 3 weeks of culture on an Axio Observer.Z1 (Zeiss) in bright-field mode with 5x or 10x magnification.

Cell viability

Cell viability assay was performed as previously described.[39] In short, the samples at day 0, day 2, and day 7 of culture were incubated for 45 minutes in FluoroBrite DMEM supplemented with 5 µg/mL of Hoechst 33342 (Invitrogen), 8 µM of calcein AM (Invitrogen), and 0.5 µg/mL of propidium Iodide (PI, Fluka). The samples were then imaged with a Leica SP8 confocal microscope (Leica) equipped with a 25x water immersion objective. Z-stacks of 50 µm were acquired from the sample surface with 5 µm z-steps. Images were processed using Fiji. Cell viability was determined by counting Hoechst 33342 stained nuclei as total cell number and propidium iodide signal as dead cells. Due to myoblasts spread and fusion into myotubes, calcein AM could not be used as a reliable signal to count live cells.

Analysis of nuclei alignment

Samples were stained, as described above, with Hoechst 33342 (Invitrogen) and calcein AM (Invitrogen) after 7 days of culture. Images were taken aligning the microstrands vertically. Using the software Fiji, the Hoechst 33342 channel was used to identify the nuclei by applying a Gaussian blur filter, followed by thresholding to create a binary image, and finally by using the watershed method to separate close nuclei. The segmented objects were then analyzed with the Extended Particle Analyzer function to evaluate nuclei angle and circularity distributions. Data were plotted using Prism 8 (GraphPad).

Immunofluorescence

After 3 weeks in culture, samples were washed 3x in PBS and fixed in 4% paraformaldehyde for 4 h at room temperature followed by 3x washing in PBS supplemented with 0.02% BSA. Samples were then permeabilized using a solution of 1% Triton-X100 in PBS for 10 minutes, followed by 3x washing in PBS + 0.02% BSA. After a blocking step using 1% BSA, 1% Tween-20 solution in PBS for 30 minutes, the constructs were incubated with primary anti-human myosin heavy-chain antibody (MF-20, DHSB), diluted 1:20 in PBS overnight. After 3x washing in PBS, the constructs were incubated with fluorescent secondary antibody (goat anti-mouse Alexa488, Invitrogen) and Hoechst 33342 (Invitrogen), both diluted 1:1000 in PBS in the presence of 0.02% BSA for 2 hours. Imaging was performed on Leica SP8 confocal microscope (Leica), equipped with a 25x water immersion objective.

For ki-67 staining, samples were treated as described above up to the blocking step and then incubated with anti ki-67 antibody (550609, BD) diluted 1:200 in PBS overnight. After 3x washes, samples were incubated with the Alexa 488 secondary antibody anti-mouse and Hoechst

as described previously. Imaging was performed on Leica SP8 confocal microscope (Leica), equipped with a 40x water immersion objective.

For actin staining, samples were treated as described above, washed 3x in PBS and incubated for 2 hours at room temperature in a solution containing Hoechst 33342 (1:1000 dilution) and Phalloidin-TRITC (0.13 µg/ml in 1% PBS-BSA, P1951, Sigma). After 3x washing with PBS, the samples were imaged on Leica SP8 equipped with 40x water immersion objective.

Gene expression analysis

RNA was extracted from samples with NucleoZol (Macherey-Nagel) according to the manufacturer's instructions. Retrotranscription to cDNA was performed with GoScript Reverse Transcriptase (Promega) and subsequently diluted 1:5 with RNAse-free water for qPCR analysis. Analysed genes were MyoD (Fw: AAGACGACTCTCACGGCTTG, Rv: CGGGGCCTGTCAAGTCTATG) MyoG (Fw: AGCCCAGCGAGGGAATTTAG, Rv: GGGACATTAACAAGGGGGCT), MyH1 (Fw: CATCCCTAAAGGCAGGCTCT, Rv: GACTTCCGGAGGTAAGGAGC), Pax7 (Fw: CCCATGGTTGTGTCTCCAAGAT, Rv: CGGAGTCGCCACCTGTCTG), all compared to GAPDH expression as housekeeping gene (Fw: GGTGAAGGTCGGTGTGAACGGATTTGG, Rv: GGTCAATGAAGGGGTCGTTGATGGCAAC). qPCR was performed with GoTaq PCR (Promega) on a QuantStudio 3 device (Applied Biosystems).

3. Results and Discussion

3.1 Sizing process and choice of the material

Physical guidance of cells by means of oriented hydrogel microarchitecture represents an attractive solution for tissue engineering of naturally aligned tissues, such as muscles and tendons. The presence of physical cues can provide preferential directionality for cell spreading and migration, eventually having an impact on cell differentiation and tissue functionality. Importantly, this organized cellular alignment should be induced not only on the surface of the scaffold, but also in its depth. In fact, although many successful studies on the effect of structural patterns were conducted on 2D systems,[45-46] 3D structural guidance remains a challenge. In this work, an easy method to generate macroporous hydrogel constructs with aligned microstructures for 3D cellular alignment is presented.

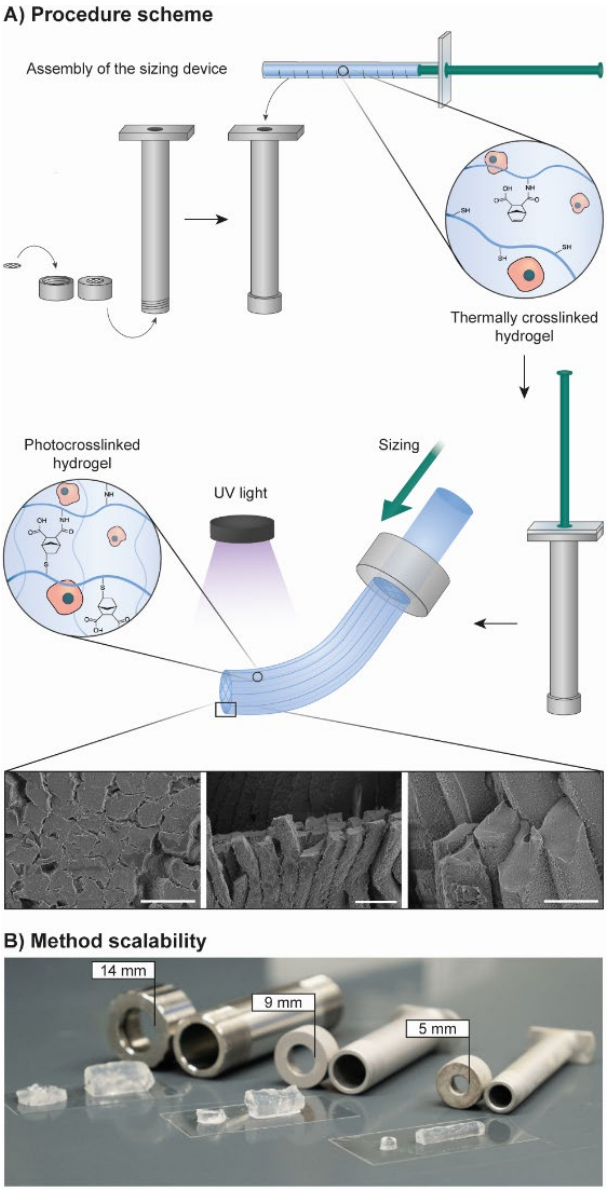

Figure 1. Sizing process. A) Illustration of the procedure. On top, the assembly of the sizing device is shown with nylon grid, syringe, and mesh metal holders and the syringe filled with cell-laden photoresin based on Gel-NB/Gel-SH. Upon cooling to obtain a thermally reversible gel, the cell-laden hydrogel is pushed through the grid to obtain a hydrogel construct composed of aligned cellular microstrands. The latter is then stabilized via UV exposure, triggering photoclick thiol-norbornene reactions. At the bottom, a close-up with SEM images of the aligned microstrands forming the sized gel. Scale bar: 50 µm. B) Sized gels of various dimensions (cross

section and entire gel) on glass slides. On the side, devices used to show the method scalability. From left to right: 10-mL, 3-mL, and 1-mL device. Labels refer to the aperture of the grid holder, which in turns reflects the final gel diameter.

As illustrated in Figure 1A, this method is based on the deconstruction of a bulk hydrogel into long, aligned microstrands with tunable dimension by sizing it through a grid of variable opening sizes. The microstrand construct was then stabilized with a secondary UV crosslinking process. As a proof of concept, aligned microstrands were generated starting with 1, 3, or 10 mL of photosensitive material (photoresin) using sizing devices of various dimensions, thus showing the scalability of the method (Figure 1B). A material suitable for such sizing process should be able to undergo a first crosslinking step in the syringe to form a bulk hydrogel and a second one after the sizing procedure to stabilize the construct. This could be achieved with a variety of methods, ranging from physical or ionic crosslinking,[47-49] to enzymatic,[50-51] or to photocrosslinking.[16] To fulfill this requirement, we used a combination of gelatin-norbornene (Gel-NB) and gelatin-thiol (Gel-SH) as a model system in this work (Figure 1A). Gelatin represents one of the most widely used biopolymers in the field of bioprinting and tissue engineering due to its biocompatibility, bioactivity (i.e., presence of RGD adhesion sites), biodegradability, and low cost.[52-55] It has intrinsic reversible thermal gelation properties, and it is relatively easy to functionalize with reactive moieties. We exploited the gelatin thermoreversible physical gelation induced by cooling as a first crosslinking strategy and introduced the highly efficient photoclick thiol-norbornene reaction as the secondary crosslinking strategy. In recent years, thiol-ene chemistry appeared to be a more attractive solution for biomedical applications when compared to traditional chain-growth polymerization (i.e., methacryloyl derivatives such as Gel-MA), due to its faster reaction kinetic which reduces the need for long light exposures and

free-radical formation.[56-59] Among the various advantages, the click-like reaction also leads to a more homogenous network formation than the one formed with the growth of a hydrophobic kinetic chain of chain-growth systems. In this study, Gel-NB (DS: 0.163 ± 0.003 mmol/g) and Gel-SH (DS: 0.276 ± 0.016 mmol/g) (Figure S1, S2, S3, see Supporting Information) were combined to have equimolar amount of the reactive groups for a total polymer concentration of 2%, 5%, or 10%. For every formulation, the state-of-the-art water soluble photoinitiator LAP was used at a final concentration of 0.05%, as was proven to be highly biocompatible in previous works.[39, 60-61]

3.2 Macroporosity and percolation

The effects of four different commercially available nylon grids with opening sizes of 20 μm, 40 μm, 70 μm, and 100 μm were investigated in comparison with common monolithic bulk hydrogel (Figure 2A). The sizing process was shown to lead to the formation of aligned high aspect ratio microstrands with tunable dimensions reflecting the opening size (Figure 2B). The presence of such anisotropic microarchitecture was observed also within the construct, indicating a potential for 3D physical guidance.

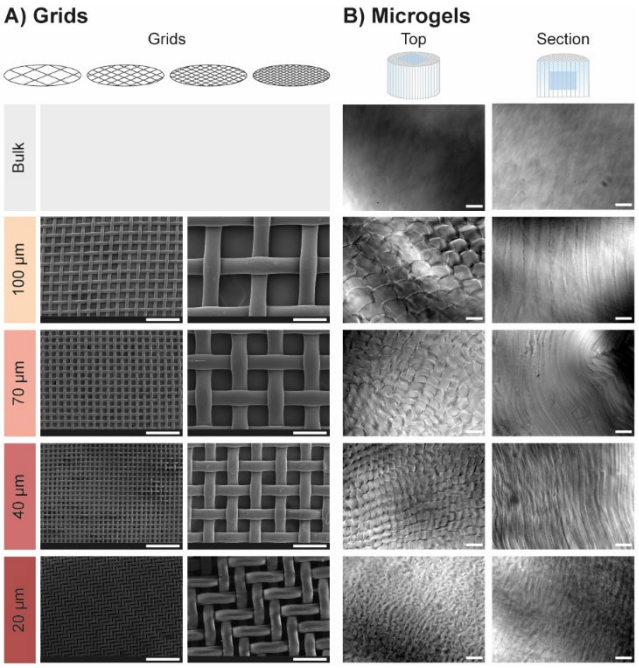

Figure 2. Grids and sized gels. A) SEM images of nylon grids of various openings size. For the bulk gel no grid was used. Scale bar: left 500 µm, right 100 µm. B) Brightfield images of sized gels showing aligned microstrand structures with variable size from the top (left) and from the side in an inner section (right). Scale bar: 100 µm.

Notably, it was observed that the sizing process generated macropores between the elongated microstrands, thus significantly enhancing the biological relevance of this system (Figure 3). In fact, the porosity of a scaffold is a pivotal aspect for the sufficient transport of nutrients and oxygen and the removal of catabolic waste. The presence of micrometer-sized void spaces can also facilitate cell infiltration and migration,[30, 62-64] and this is commonly referred to as macroporosity for pore diameters in the range of ~0.1-10 µm and supermacroporosity for pore cross-sections ranging from tens to hundreds of micrometers.[65] The latter term is, however, almost exclusively found to describe cryogels.[66-68] Bulk hydrogels' porosity is instead commonly referred to as nanoporosity, due to the fact that the intricate crosslinked mesh of polymer chains leaves pores in the range of nanometers.[69-72] Such a dense network strongly limits mass transport,

which is therefore restricted to a limited diffusion distance (~100-200 μm), a major obstacle in the tissue engineering field of millimeter- to centimeter-sized structures.[73] To assess the formation of macroporous structures, the sized gels were submerged into a solution of fluorescent, high molecular weight dextran (FITC-Dextran). Confocal imaging revealed the presence of elongated macropores running along the interfaces between proximal microstrands, while there was complete absence of percolation (fluid movement through porous material) in the bulk gel (Figure 3A). Because the use of smaller grids results in more numerous microstrands, the total porosity appeared to be inversely correlated to the grid size. The 20-μm and 40-μm grids showed a porosity of ~25%, while for the bigger 70-μm and 100-μm grids, the void fraction was ~15% and ~8%, respectively (Figure 3B). On the other hand, the pores' size seemed to have a less pronounced correlation to the grid openings' size, although larger pores are more likely to be found with the bigger grids. Pore size is, in fact, most probably dependent on the dimensions of nylon fibers, which are found to be larger (45 μm versus 30 μm) and thicker (60 μm versus 45 μm) for the 100- and 70-μm grids when compared to the 20- and 40-μm (Figure 2A). As a result, the sized constructs showed a pore size ranging from a minimum average of ~190 μm^2 for the 20-μm grid to a maximum average of ~526 μm^2 for the 70-μm grid (Figure 3C). Such void spaces create an ideal percolating system throughout the whole construct, which facilitates mass transport, thereby overcoming the diffusion distance barrier and creating an excellent environment for cell infiltration.

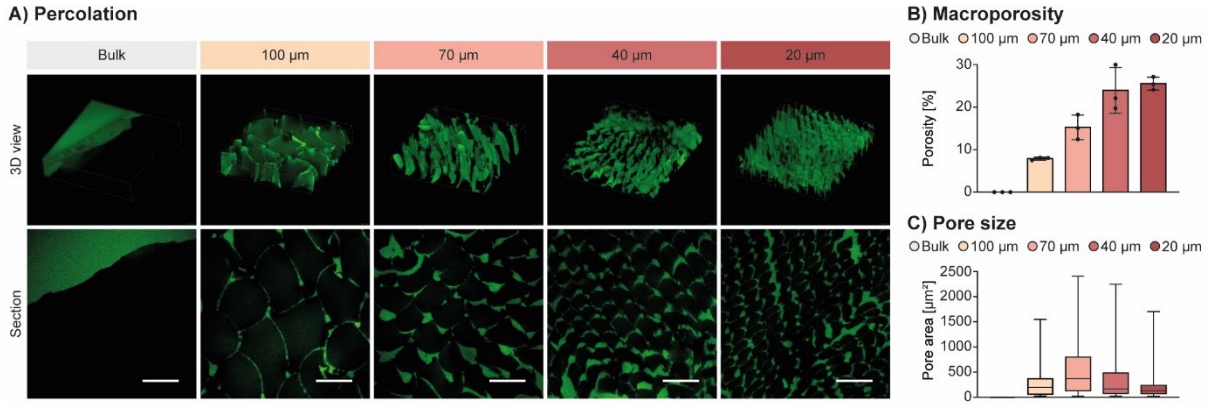

Figure 3. Macroporosity. A) Confocal images of fluorescent high molecular weight dextran (FITC-dextran) percolating into the aligned macropores found between proximal microstrands. For the bulk gel, no percolation was observed, due to absence of macroporosity. The fluorescent signal comes from the FITC-dextran solution around the gel itself. On top, a 3D volume reconstruction of a 100-µm z-stack. At the bottom, a 2D section of the porous constructs. Scale bar: 100 µm. B) Sized gel macroporosity reported as percentage of void fraction showing a tendency towards higher porosity for smaller grid size. C) Average pore size for various sized constructs with a distribution ranging from ~20 μm^2 to over 2000 μm^2. Macropores were instead not found in the bulk gel.

3.3 Computational modeling and cell viability

To gain more insights into the effect of the sizing process on cell viability, which relies on the application of mechanical forces to sieve the bulk hydrogel through the grid, we ran a finite element analysis (FEA) and compared these results with an *in vitro* viability assay. First, to better model the sizing process for our Gel-NB/Gel-SH formulation, rheological tests were performed to extrapolate storage modulus, yield stress, and viscosity of thermally crosslinked 2%, 5% and 10% photoresins (Figure 4A). The physically crosslinked gelatin-based hydrogel storage modulus ranged from ~270 Pa for the soft 2% condition to ~3.4 kPa and ~11.4 kPa for

the much stiffer 5% and 10% gels, respectively (Figure 4A, top). Yield stress, determined as the peak value of elastic stress obtained with a strain sweep, also followed the same trend, spanning from ~588 Pa for 2%, to ~11.5 kPa and ~28.7 kPa for 5% and 10%, respectively (Figure 4A, middle). Shear thinning tests were used to determine the initial viscosity and flow behavior index of the different hydrogels (Figure 4A, bottom).

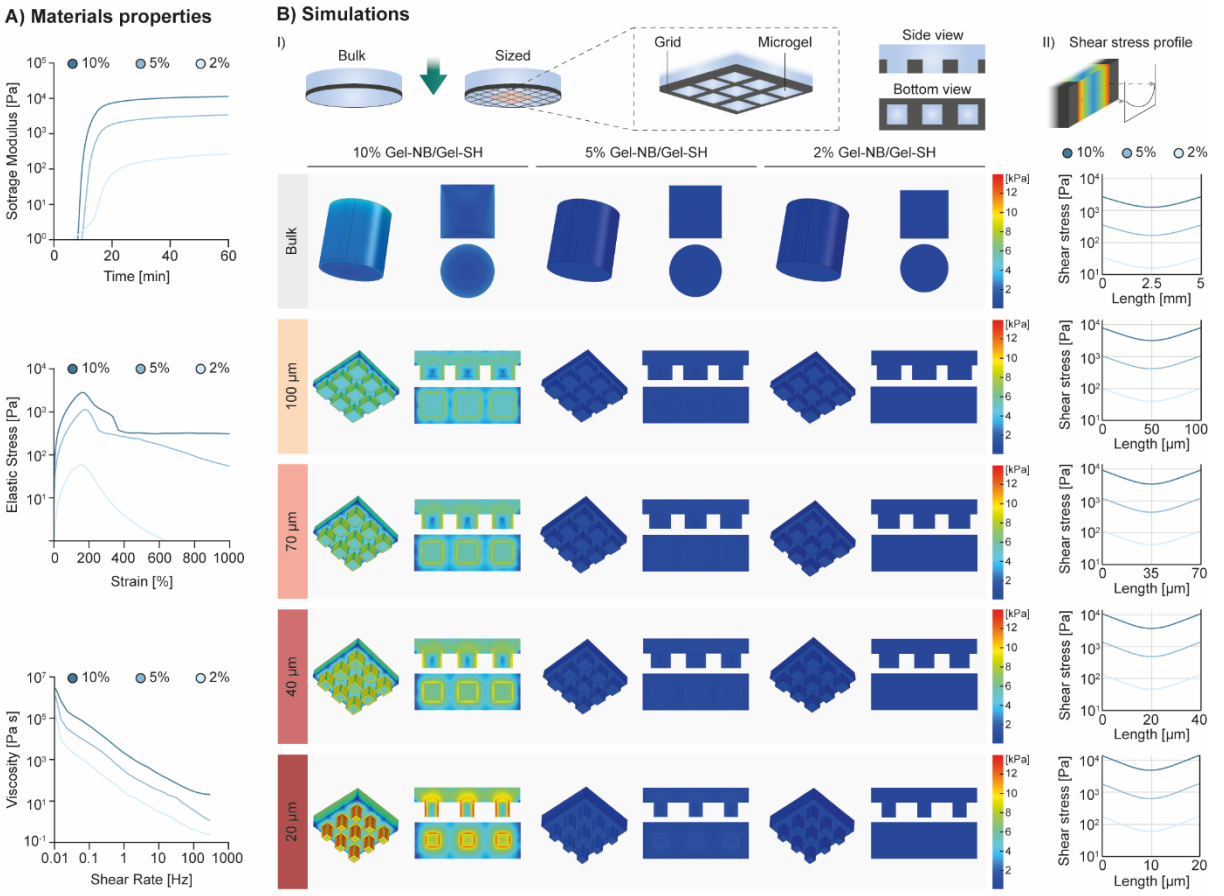

Figure 4. Computational modeling of the sizing of Gel-NB/Gel-SH thermally-crosslinked hydrogels. A) Rheological measurements used to determine the storage moduli (top), yield stress (middle) and viscosity (bottom) of the material to be used for the computational models. All the photoresin concentrations tested demonstrated a shear thinning characteristic following the power law (Equation 1, see Materials and methods) with a flow behavior index of 0.2 and flow consistency indices of 22, 229, and 1750 Pa s for 2%, 5%, and 10% concentrations, respectively.

B) (I) Color-coded output of shear stress determined by an inelastic non-Newtonian flow model in COMSOL (see Materials and method section). Results are shown for the whole bulk gel (without sizing grid), and 3×3 mesh of the sizing grid for sized constructs, as illustrated on the top row. Simulation results are presented in 3D view, side cross section and bottom cross section, as illustrated on the top row. For clarity, the nylon grids are not shown in the simulations. (II) Shear stress distribution in a single-forming microstrand, illustration (top) and results plotted for the bulk condition and the different grid sizes. The profiles showed a clear increase in shear stress for stiffer hydrogels (higher polymer concentration) and smaller grid size. In all the conditions the shear stress was found to be highest on the periphery of the microstrands.

As expected, polymer concentration plays a central role in the induced shear stress. Due to the larger photoresin viscosity and stiffness, the computational modeling showed that the shear stress for the 10% condition (max ~12 kPa) was an order of magnitude higher than 5% (max ~1.6 kPa) and two orders of magnitude higher than for 2% (max ~155 Pa). In addition, the simulations revealed a correlation between the grid openings' size and shear stress magnitude. Smaller grids were in fact found to induce the highest shear stress for each photoresin formulation. For the bulk gel, where no grid was used, the shear stress was found be significantly lower (max ~4 kPa for 10%, ~550 Pa for 5%, and ~50 Pa for 2%) and confined only to the outer periphery of the tube where the no-slip boundary condition applies.[74] For the sized gels, due to the same concept of no-slip boundary, the highest shear stress values were reported at the periphery of the single opening of the sizing grid and showed to be more pronounced for smaller grid sizes. This phenomenon could be attributed to the increased fluid flow velocity in the smaller opening due to a constrained volume. A detailed distribution of the shear stress for a single microstrand within a single grid opening (or the whole bulk hydrogel in the syringe) is reported in Figure

4BII. In short, from the *in silico* analysis, it can be inferred that a combination of high polymer content and small sizing grid will lead to the worst conditions in terms of shear stress experienced by encapsulated cells, which would eventually affect the viability of the construct. On the other hand, sizing of soft, low-polymer-content hydrogels is expected to have no or negligible harmful effects. Extensive investigation on shear stress-induced cell damage in the bioprinting field found a threshold around 5 kPa, above which cell survival tends to be significantly reduced.[75-76] Other studies set the bar of critical stress much lower (~250-500 Pa).[77-78] Therefore, the 2% condition appears to be the most likely to result in a satisfying biocompatibility output.

The results of the simulations were compared to cell viability of C2C12 myoblasts sized under the same conditions (Figure 5). Specifically, sizing of cell-laden Gel-NB/Gel-SH thermally crosslinked hydrogels was conducted, varying the grid size (20 μm, 40 μm, 70 μm, 100 μm, and bulk) and polymer concentration (2%, 5%, and 10%). For every condition, the viability was determined in the outer part of the gel (surface) and the inner part of the gel. The latter was performed by cutting the gel in half prior to imaging, allowing for the assessment of this method's potential to truly guide cellular alignment in 3D (Figure 5A). As predicted by the FEA simulation, higher polymer concentrations (5% and 10%), which are associated with higher shear stress, led to extensive cell death at day 0 immediately after the extrusion (Figure 5B). The viability only partially recovered in the following days, both in the inner and outer parts of the constructs. In particular, the conditions that were predicted to be the harshest (10% polymer concentration, 20-40 μm grids) showed an almost complete absence of viable cells after one week (Figure S4A, Supplementary Information). However, for the 5% hydrogels, the cells that were not irreversibly damaged during the sizing procedure proliferated in both the inner and

outer parts of the constructs (Figure S4B, Supplementary Information) as also confirmed by the presence of ki-67 positive cells (Figure S5, Supporting Information). Finally, as expected based on simulations, polymer concentration of 2% yielded the best result, with excellent cell viability (>90%) immediately after sizing and during the first week of culture. Although high viability at day 0 can be attributed to low shear stress, its retention during the 7 days of culture probably depends on the hydrogel mechanical properties and the generated microarchitecture. On one hand, after the stabilizing photocrosslinking step, the compressive modulus for the Gel-NB/Gel-SH constructs was reported to be ~ 4.7 kPa for 2%, ~ 10 kPa for 5%, and ~32 kPa for 10% (Figure 5C). Matrix stiffness has in fact been shown to strongly influence C2C12 spreading and differentiation, with better output for softer gels.[79] On the other hand, as evidenced in the previous paragraph, the sizing process facilitates mass transports within the construct due to the presence of aligned macropores in between the formed microstrands. This provides more nutrients and space for the cells to grow in the inner part of the gel compared to the bulk condition, as could be inferred by the drop in cell viability for such monolithic constructs after 2 days. Recovery in cell viability for the bulk gel (inner part) at day 7 appears instead artificially high. At this time point, due to the drastic decrease in cell number reported after day 2 (see Figure S6, Supporting Information), the percentage of the few remaining live cells becomes similar to the one of the other conditions.

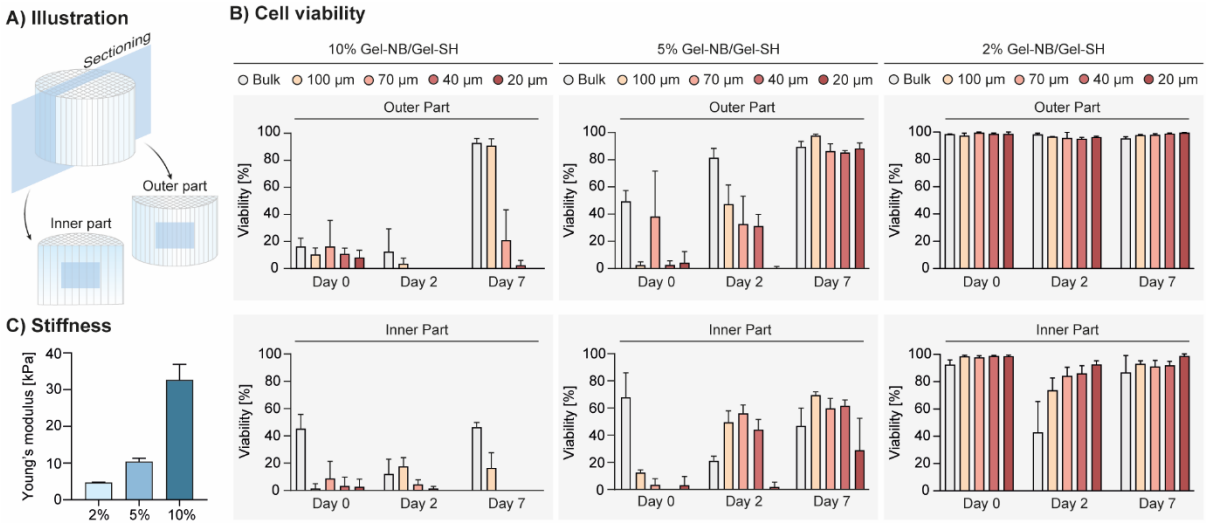

Figure 5. Viability assay. A) Schematic depicting the imaging procedure, taking into account both the surface of the hydrogels (outer part) and the core (inner part) to verify the impact of the aligned microstrands within the whole 3D construct. B) Cell viability determined at day 0 (immediately after extrusion), day 2 and day 7 of 10%, 5%, and 2% Gel-NB/Gel-SH hydrogels sized with the various grids. C) Compressive (Young's) modulus of the hydrogels after the stabilizing secondary crosslinking via UV exposure.

3.4 3D physical guidance of oriented cell maturation

Using a Gel-NB/Gel-SH concentration of 2%, which was found to be the optimal condition both *in silico* and *in vitro*, the cell guidance potential of the microstrands was investigated. Importantly, also in this case both the surface of the gel (outer part) and its core (inner part) were analyzed, to have a complete view on cell behavior in the 3D constructs. Muscle tissue is a good example of highly aligned tissue, with fiber alignment playing a crucial role in dictating its mechanical function (muscle contraction). Tissue engineered muscle constructs that are able to mimic the native microarchitecture can be used as functional *in vitro* models,[80-84] and they are seen as a promising treatment for muscle traumas or disorders such as volumetric muscle loss

(VML),[85-86] and sarcopenia.[87-88] In this study, mouse myoblasts (C2C12) were used as a proof-of-concept model to test the method's ability to generate aligned skeletal muscle tissues. C2C12 cells were found to be highly viable (Figure 5B) and homogeneously distributed upon sizing at day 0 (Figure 6A). After one week, a clear preferential orientation was observed along the direction of the microstrands. On the surface, myoblasts fused to form multinucleated myotubes which were oriented parallel to the microstrands. As expected, this phenomenon was found to be less pronounced for the bulk gel, where a plain surface did not induce a favored orientation for cellular alignment.

Interestingly, a more pronounced difference was found when comparing the inner part of the constructs. In the bulk gel a clear reduction in viable cells was shown, in accordance with the drastic cell death reported upon two days of culture (Figure 5B). Also, for the bulk gel, the cellsmaintained a round shape, suggesting the absence of spreading and migration and consequently the absence of myotubes, whose formation depends on the ability of cells to come into close contact with each other (Figure 6B). For the sized constructs, on the other hand, the presence of the physical cues represented by the aligned microstrands and the aligned macropores induced marked cell alignment (Figure S7, Supporting Information). Myoblasts were mainly observed on the surface of the microstrands, where macropores were found, indicating that the cells had migrated from the hydrogel into the void spaces. These findings, together with the better cell viability of sized constructs compared to the bulk condition in the inner part of the gel, show that our method contributes to a drastic enhancement of oriented 3D cell guidance and viability. On one hand, the presence of macropores facilitates media percolation and creates a favourable niche for cell infiltration and migration overcoming the limit of the diffusion

distance; on the other hand, high-aspect ratio-aligned microstrands provide a preferred growth direction.

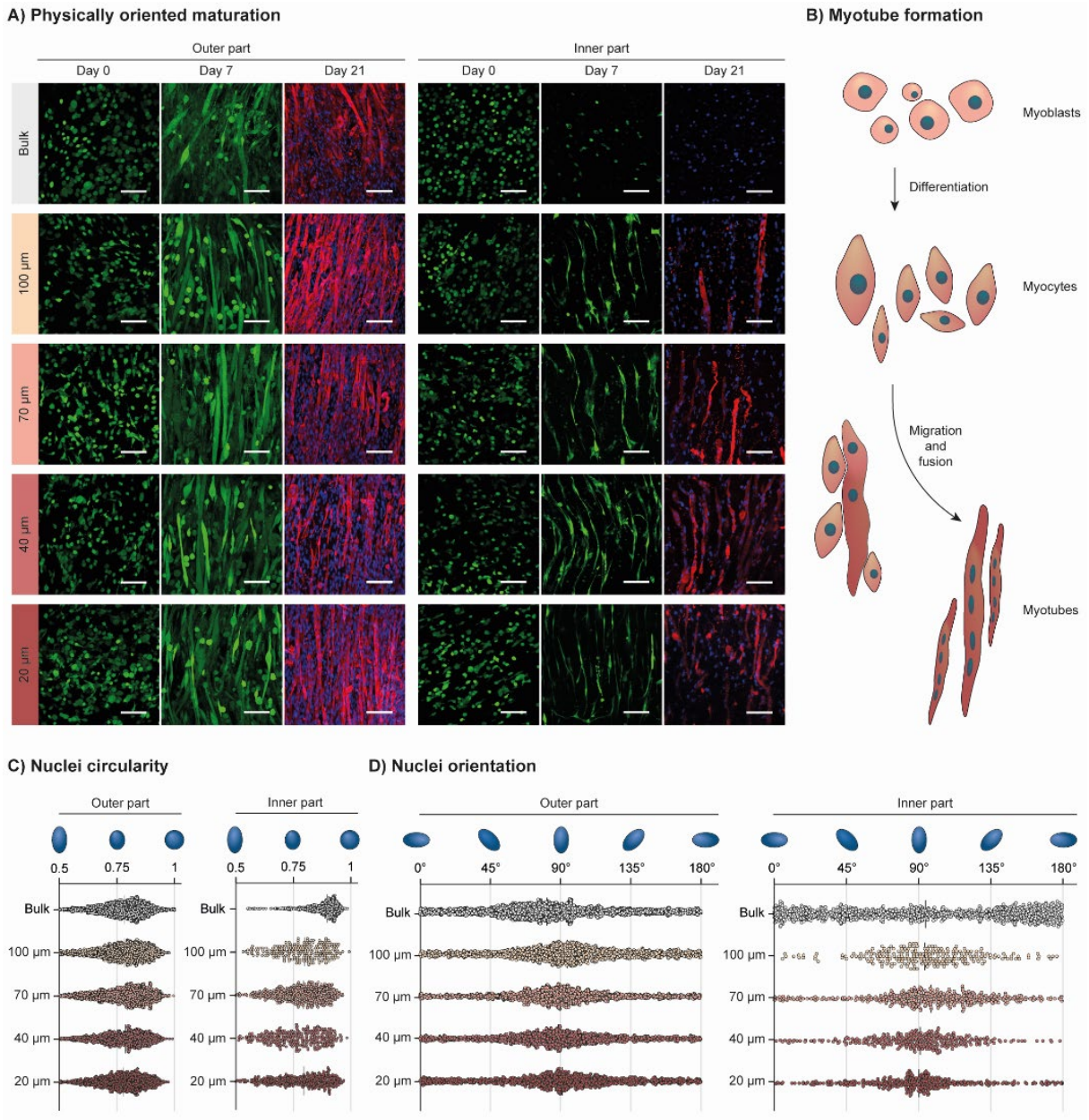

Figure 6. 3D physical cell guidance. A) Calcein AM staining (green) of the outer part (left) and inner part (right) of bulk and sized constructs at day 0 and day 7 showing oriented tissue development. In red, immunofluorescence myosin heavy chain staining after 21 days showing maturation into myotubes. The bulk gel did not provide a suitable 3D environment for myoblast

maturation and alignment, especially on the inner part. Scale bar: 100 μm. B) Illustration of myotube formation with alignment of nuclei along cell orientation and reduction in nuclei circularity. C) Nuclei circularity in outer and inner part of bulk and sized constructs after 7 days of culture. A clear difference is shown for internal bulk gel, where nuclei remain substantially round, suggesting no cell maturation. D) Nuclei orientation in outer and inner part of bulk and sized constructs after 7 days of culture. Within the bulk gel, where no macropores and physical cues were present, a random nuclei orientation reflects absence of cell alignment and myotube formation.

To further evaluate the possibility of creating physiologically relevant models, we cultured the constructs for three weeks and stained them for myosin heavy chain (MHC). Immunofluorescence confirmed differentiation into multinucleated myotubes (Figure 6A) which were also found to be contractile (Video S2, Supporting Information), both in the outer part and in the inner part of the gels. Again, for the homogeneous bulk hydrogel, no formation of MHC positive myotubes was observed in the inner part. Cells were also shown to differentiate by means of gene expression analysis (Figure S8, Supporting Information). Common markers for myoblast differentiation MyoD, MyoG and MyoH1 were found to be increasingly expressed over time. Also, expression of Pax7 after 3 weeks of culture indicates that a fraction of cells possibly returned to a quiescent state, reminiscent of satellite cells responsible for homeostasis and repair of the muscle tissue. To quantify cell alignment in our C2C12 model system, we evaluated nucleus circularity and nucleus orientation. When elongated multinucleated myotubes are formed, the nuclei tend to assume an oval shape (circularity <1) and align along the major axis of the myotube (Figure 6B).[89-94] In accordance with the qualitative observation of Figure 6A, nuclei were found to be more elongated in all the conditions, with the exception of the inner

part of the bulk gel (Figure 6C). In this case the nucleus circularity was found to be close to 1, as expected for non-differentiated round cells. Nucleus orientation was also found to confirm the presence of aligned myotubes in all the conditions, with the exception of the inner part of the bulk gel (Figure 6D).

4. Conclusions

We have developed and optimized a simple method of generating large (mm to cm) macroporous anisotropic constructs with aligned physical cues to induce oriented cell alignment. Although we used myoblasts for proof of concept, we foresee that the promising results obtained with such cells will encourage the generation of more complex, multicellular constructs of aligned tissues. In addition, in this study we adopted the thermal crosslinking of gelatin as primary crosslinking and the highly efficient photoclick thiol-norbornene reaction as secondary crosslinking. However, other natural or synthetic polymers and different crosslinking strategies can be applied to tailor the materials' mechanical or bioactive properties to specific needs. Finally, exploring the effects of different grid geometries (i.e., circular or star-shaped openings) in tuning the shape, size and proportion of microstrands and macropores can broaden the potential of the technique presented in this work.

Supporting Information.

The following files are available free of charge.

Supplementary Figures including synthesis schemes, NMR spectra, CalceinAM stainings, ki-67 immunofluorescence, cell count, actin staining and gene expression analysis. (PDF)

Supplementary Video S1 (mp4)

Supplementary Video S2 (mp4)

Corresponding Author

* E-mail: marcy.zenobi@hest.ethz.ch

Author Contributions

The manuscript was written through contributions of all authors. All authors have given approval to the final version of the manuscript. ‡These authors contributed equally.

Declaration of competing interests

The authors declare no competing financial interest

Acknowledgments

The authors would like to thank Peter Schwilch for the help in the design and production of the sizing devices. The authors further acknowledge the assistance from the ETH imaging facilities (ScopeM).

REFERENCES

1. Fu, J.; in het Panhuis, M., Hydrogel properties and applications. *Journal of Materials Chemistry B* **2019,** *7* (10), 1523-1525, DOI: 10.1039/C9TB90023C

2. Ramiah, P.; du Toit, L. C.; Choonara, Y. E.; Kondiah, P. P. D.; Pillay, V., Hydrogel-Based Bioinks for 3D Bioprinting in Tissue Regeneration. *Frontiers in Materials* **2020,** *7*, DOI: 10.3389/fmats.2020.00076

3. Bedell, M. L.; Navara, A. M.; Du, Y.; Zhang, S.; Mikos, A. G., Polymeric Systems for Bioprinting. *Chemical Reviews* **2020,** *120* (19), 10744-10792, DOI: 10.1021/acs.chemrev.9b00834

4. Mota, C.; Camarero-Espinosa, S.; Baker, M. B.; Wieringa, P.; Moroni, L., Bioprinting: From Tissue and Organ Development to in Vitro Models. *Chemical Reviews* **2020,** *120* (19), 10547-10607, DOI: 10.1021/acs.chemrev.9b00789

5. Lutzweiler, G.; Ndreu Halili, A.; Engin Vrana, N., The Overview of Porous, Bioactive Scaffolds as Instructive Biomaterials for Tissue Regeneration and Their Clinical Translation. *Pharmaceutics* **2020,** *12* (7), DOI: 10.3390/pharmaceutics12070602

6. Annabi, N.; Nichol, J. W.; Zhong, X.; Ji, C.; Koshy, S.; Khademhosseini, A.; Dehghani, F., Controlling the Porosity and Microarchitecture of Hydrogels for Tissue Engineering. *Tissue Engineering Part B: Reviews* **2010,** *16* (4), 371-383, DOI: 10.1089/ten.teb.2009.0639

7. De France, K. J.; Xu, F.; Hoare, T., Structured Macroporous Hydrogels: Progress, Challenges, and Opportunities. *Advanced Healthcare Materials* **2018,** *7* (1), 1700927, DOI: 10.1002/adhm.201700927

8. Hamley, I. W., Small Bioactive Peptides for Biomaterials Design and Therapeutics. *Chemical Reviews* **2017,** *117* (24), 14015-14041, DOI: 10.1021/acs.chemrev.7b00522

9. Caballero Aguilar, L. M.; Silva, S. M.; Moulton, S. E., Growth factor delivery: Defining the next generation platforms for tissue engineering. *Journal of Controlled Release* **2019,** *306*, 40-58, DOI: 10.1016/j.jconrel.2019.05.028

10. Huettner, N.; Dargaville, T. R.; Forget, A., Discovering Cell-Adhesion Peptides in Tissue Engineering: Beyond RGD. *Trends in Biotechnology* **2018,** *36* (4), 372-383, DOI: 10.1016/j.tibtech.2018.01.008

11. Li, J.; Liu, Y.; Zhang, Y.; Yao, B.; Enhejirigala; Li, Z.; Song, W.; Wang, Y.; Duan, X.; Yuan, X.; Fu, X.; Huang, S., Biophysical and Biochemical Cues of Biomaterials Guide Mesenchymal Stem Cell Behaviors. *Frontiers in Cell and Developmental Biology* **2021,** *9*, DOI: 10.3389/fcell.2021.640388

12. Broguiere, N.; Lüchtefeld, I.; Trachsel, L.; Mazunin, D.; Rizzo, R.; Bode, J. W.; Lutolf, M. P.; Zenobi-Wong, M., Morphogenesis Guided by 3D Patterning of Growth Factors in Biological Matrices. *Advanced Materials* **2020,** *32* (25), 1908299, DOI: 10.1002/adma.201908299

13. Farrukh, A.; Paez, J. I.; del Campo, A., 4D Biomaterials for Light-Guided Angiogenesis. *Advanced Functional Materials* **2019,** *29* (6), 1807734, DOI: 10.1002/adfm.201807734

14. Qin, X.-H.; Wang, X.; Rottmar, M.; Nelson, B. J.; Maniura-Weber, K., Near-Infrared Light-Sensitive Polyvinyl Alcohol Hydrogel Photoresist for Spatiotemporal Control of Cell-Instructive 3D Microenvironments. *Advanced Materials* **2018,** *30* (10), 1705564, DOI: 10.1002/adma.201705564

15. Lee, S.-H.; Moon, J. J.; West, J. L., Three-dimensional micropatterning of bioactive hydrogels via two-photon laser scanning photolithography for guided 3D cell migration. *Biomaterials* **2008,** *29* (20), 2962-2968, DOI: 10.1016/j.biomaterials.2008.04.004

16. Lee, M.; Rizzo, R.; Surman, F.; Zenobi-Wong, M., Guiding Lights: Tissue Bioprinting Using Photoactivated Materials. *Chemical Reviews* **2020,** *120* (19), 10950-11027, DOI: 10.1021/acs.chemrev.0c00077

17. Schuldiner, M.; Yanuka, O.; Itskovitz-Eldor, J.; Melton, D. A.; Benvenisty, N., Effects of eight growth factors on the differentiation of cells derived from human embryonic stem cells. *Proceedings of the National Academy of Sciences* **2000,** *97* (21), 11307-11312, DOI: 10.1073/pnas.97.21.11307

18. Ma, J.; Huang, C., Composition and Mechanism of Three-Dimensional Hydrogel System in Regulating Stem Cell Fate. *Tissue Engineering Part B: Reviews* **2020,** *26* (6), 498-518, DOI: 10.1089/ten.teb.2020.0021

19. Lutolf, M. P.; Hubbell, J. A., Synthetic biomaterials as instructive extracellular microenvironments for morphogenesis in tissue engineering. *Nature Biotechnology* **2005,** *23* (1), 47-55, DOI: 10.1038/nbt1055

20. Hersel, U.; Dahmen, C.; Kessler, H., RGD modified polymers: biomaterials for stimulated cell adhesion and beyond. *Biomaterials* **2003,** *24* (24), 4385-4415, DOI: 10.1016/S0142-9612(03)00343-0

21. Heino, J., The collagen family members as cell adhesion proteins. *BioEssays* **2007,** *29* (10), 1001-1010, DOI: 10.1002/bies.20636

22. Li, P.; Dou, X.; Feng, C.; Schönherr, H., Enhanced cell adhesion on a bio-inspired hierarchically structured polyester modified with gelatin-methacrylate. *Biomaterials Science* **2018,** *6* (4), 785-792, DOI: 10.1039/C7BM00991G

23. Davidenko, N.; Schuster, C. F.; Bax, D. V.; Farndale, R. W.; Hamaia, S.; Best, S. M.; Cameron, R. E., Evaluation of cell binding to collagen and gelatin: a study of theeffect of 2D and 3D architecture and surface chemistry. *Journal of Materials Science: Materials in Medicine* **2016,** *27* (10), 148, DOI: 10.1007/s10856-016-5763-9

24. Rose, J. C.; Gehlen, D. B.; Omidinia-Anarkoli, A.; Fölster, M.; Haraszti, T.; Jaekel, E. E.; De Laporte, L., How Much Physical Guidance is Needed to Orient Growing Axons in 3D Hydrogels? *Advanced Healthcare Materials* **2020,** *9* (21), 2000886, DOI: 10.1002/adhm.202000886

25. Leclech, C.; Villard, C., Cellular and Subcellular Contact Guidance on Microfabricated Substrates. *Frontiers in Bioengineering and Biotechnology* **2020,** *8*, DOI: 10.3389/fbioe.2020.551505

26. Gasiorowski, J. Z.; Murphy, C. J.; Nealey, P. F., Biophysical Cues and Cell Behavior: The Big Impact of Little Things. *Annual Review of Biomedical Engineering* **2013,** *15* (1), 155-176, DOI: 10.1146/annurev-bioeng-071811-150021

27. Kim, T. H.; An, D. B.; Oh, S. H.; Kang, M. K.; Song, H. H.; Lee, J. H., Creating stiffness gradient polyvinyl alcohol hydrogel using a simple gradual freezing–thawing method to investigate stem cell differentiation behaviors. *Biomaterials* **2015,** *40*, 51-60, DOI: 10.1016/j.biomaterials.2014.11.017

28. Guilak, F.; Cohen, D. M.; Estes, B. T.; Gimble, J. M.; Liedtke, W.; Chen, C. S., Control of Stem Cell Fate by Physical Interactions with the Extracellular Matrix. *Cell Stem Cell* **2009,** *5* (1), 17-26, DOI: 10.1016/j.stem.2009.06.016

29. Engler, A. J.; Sen, S.; Sweeney, H. L.; Discher, D. E., Matrix Elasticity Directs Stem Cell Lineage Specification. *Cell* **2006,** *126* (4), 677-689, DOI: 10.1016/j.cell.2006.06.044

30. Broguiere, N.; Husch, A.; Palazzolo, G.; Bradke, F.; Madduri, S.; Zenobi-Wong, M., Macroporous hydrogels derived from aqueous dynamic phase separation. *Biomaterials* **2019,** *200*, 56-65, DOI: 10.1016/j.biomaterials.2019.01.047

31. Fereshteh, Z., 7 - Freeze-drying technologies for 3D scaffold engineering. In *Functional 3D Tissue Engineering Scaffolds*, Deng, Y.; Kuiper, J., Eds. Woodhead Publishing: 2018; pp 151-174, DOI: 10.1016/B978-0-08-100979-6.00007-0

32. Han, L.-H.; Yu, S.; Wang, T.; Behn, A. W.; Yang, F., Microribbon-Like Elastomers for Fabricating Macroporous and Highly Flexible Scaffolds that Support Cell Proliferation in 3D. *Advanced Functional Materials* **2013,** *23* (3), 346-358, DOI: 10.1002/adfm.201201212

33. Gegg, C.; Yang, F., Spatially patterned microribbon-based hydrogels induce zonally-organized cartilage regeneration by stem cells in 3D. *Acta Biomaterialia* **2020,** *101*, 196-205, DOI: 10.1016/j.actbio.2019.10.025

34. Coogan, K. R.; Stone, P. T.; Sempertegui, N. D.; Rao, S. S., Fabrication of micro-porous hyaluronic acid hydrogels through salt leaching. *European Polymer Journal* **2020,** *135*, 109870, DOI: 10.1016/j.eurpolymj.2020.109870

35. Sokic, S.; Christenson, M.; Larson, J.; Papavasiliou, G., In Situ Generation of Cell-Laden Porous MMP-Sensitive PEGDA Hydrogels by Gelatin Leaching. *Macromolecular Bioscience* **2014,** *14* (5), 731-739, DOI: 10.1002/mabi.201300406

36. Kessel, B.; Lee, M.; Bonato, A.; Tinguely, Y.; Tosoratti, E.; Zenobi-Wong, M., 3D Bioprinting of Macroporous Materials Based on Entangled Hydrogel Microstrands. *Advanced Science* **2020,** *7* (18), 2001419, DOI: 10.1002/advs.202001419

37. Aubin, H.; Nichol, J. W.; Hutson, C. B.; Bae, H.; Sieminski, A. L.; Cropek, D. M.; Akhyari, P.; Khademhosseini, A., Directed 3D cell alignment and elongation in microengineered hydrogels. *Biomaterials* **2010,** *31* (27), 6941-6951, DOI: 10.1016/j.biomaterials.2010.05.056

38. Rose, J. C.; Cámara-Torres, M.; Rahimi, K.; Köhler, J.; Möller, M.; De Laporte, L., Nerve Cells Decide to Orient inside an Injectable Hydrogel with Minimal Structural Guidance. *Nano Letters* **2017,** *17* (6), 3782-3791, DOI: 10.1021/acs.nanolett.7b01123

39. Rizzo, R.; Ruetsche, D.; Liu, H.; Zenobi-Wong, M., Optimized Photoclick (Bio)Resins for Fast Volumetric Bioprinting. *Advanced Materials* **2021,** *33* (49), 2102900, DOI: 10.1002/adma.202102900

40. Walls, H. J.; Caines, S. B.; Sanchez, A. M.; Khan, S. A., Yield stress and wall slip phenomena in colloidal silica gels. *Journal of Rheology* **2003,** *47* (4), 847-868, DOI: 10.1122/1.1574023

41. Yang, M. C.; Scriven, L. E.; Macosko, C. W., Some Rheological Measurements on Magnetic Iron Oxide Suspensions in Silicone Oil. *Journal of Rheology* **1986,** *30* (5), 1015-1029, DOI: 10.1122/1.549892

42. Zhou, M.; Lee, B. H.; Tan, Y. J.; Tan, L. P., Microbial transglutaminase induced controlled crosslinking of gelatin methacryloyl to tailor rheological properties for 3D printing. *Biofabrication* **2019,** *11* (2), 025011, DOI: 10.1088/1758-5090/ab063f

43. Chansoria, P.; Shirwaiker, R., 3D bioprinting of anisotropic engineered tissue constructs with ultrasonically induced cell patterning. *Additive Manufacturing* **2020,** *32*, 101042, DOI: 10.1016/j.addma.2020.101042

44. Chansoria, P.; Asif, S.; Gupta, N.; Piedrahita, J.; Shirwaiker, R. A., Multiscale Anisotropic Tissue Biofabrication via Bulk Acoustic Patterning of Cells and Functional Additives in Hybrid Bioinks. *Advanced Healthcare Materials* **2022,** *n/a* (n/a), 2102351, DOI: 10.1002/adhm.202102351

45. Ermis, M.; Antmen, E.; Hasirci, V., Micro and Nanofabrication methods to control cell-substrate interactions and cell behavior: A review from the tissue engineering perspective. *Bioactive Materials* **2018,** *3* (3), 355-369, DOI: 10.1016/j.bioactmat.2018.05.005

46. Abagnale, G.; Sechi, A.; Steger, M.; Zhou, Q.; Kuo, C.-C.; Aydin, G.; Schalla, C.; Müller-Newen, G.; Zenke, M.; Costa, I. G.; van Rijn, P.; Gillner, A.; Wagner, W., Surface Topography Guides Morphology and Spatial Patterning of Induced Pluripotent Stem Cell Colonies. *Stem Cell Reports* **2017,** *9* (2), 654-666, DOI: 10.1016/j.stemcr.2017.06.016

47. Xue, X.; Hu, Y.; Wang, S.; Chen, X.; Jiang, Y.; Su, J., Fabrication of physical and chemical crosslinked hydrogels for bone tissue engineering. *Bioactive Materials* **2022,** *12*, 327-339, DOI: 10.1016/j.bioactmat.2021.10.029

48. Aguero, L.; Alpdagtas, S.; Ilhan, E.; Zaldivar-Silva, D.; Gunduz, O., Functional role of crosslinking in alginate scaffold for drug delivery and tissue engineering: A review. *European Polymer Journal* **2021,** *160*, 110807, DOI: 10.1016/j.eurpolymj.2021.110807

49. GhavamiNejad, A.; Ashammakhi, N.; Wu, X. Y.; Khademhosseini, A., Crosslinking Strategies for 3D Bioprinting of Polymeric Hydrogels. *Small* **2020,** *16* (35), 2002931, DOI: 10.1002/smll.202002931

50. Berg, I.; Rizzo, R.; Lee, M.; Ren, Q.; Broguiere, N.; Zenobi-Wong, M., Factor XIII Cross-Linked Adhesive Chitosan Hydrogels. *ACS Biomaterials Science & Engineering* **2021,** *7* (6), 2198-2203, DOI: 10.1021/acsbiomaterials.1c00298

51. Broguiere, N.; Isenmann, L.; Zenobi-Wong, M., Novel enzymatically cross-linked hyaluronan hydrogels support the formation of 3D neuronal networks. *Biomaterials* **2016,** *99*, 47-55, DOI: 10.1016/j.biomaterials.2016.04.036

52. Van Hoorick, J.; Tytgat, L.; Dobos, A.; Ottevaere, H.; Van Erps, J.; Thienpont, H.; Ovsianikov, A.; Dubruel, P.; Van Vlierberghe, S., (Photo-)crosslinkable gelatin derivatives for biofabrication applications. *Acta Biomaterialia* **2019,** *97*, 46-73, DOI: 10.1016/j.actbio.2019.07.035

53. Klotz, B. J.; Gawlitta, D.; Rosenberg, A. J. W. P.; Malda, J.; Melchels, F. P. W., Gelatin-Methacryloyl Hydrogels: Towards Biofabrication-Based Tissue Repair. *Trends in Biotechnology* **2016,** *34* (5), 394-407, DOI: 10.1016/j.tibtech.2016.01.002

54. Yue, K.; Trujillo-de Santiago, G.; Alvarez, M. M.; Tamayol, A.; Annabi, N.; Khademhosseini, A., Synthesis, properties, and biomedical applications of gelatin methacryloyl (GelMA) hydrogels. *Biomaterials* **2015,** *73*, 254-271, DOI: 10.1016/j.biomaterials.2015.08.045

55. Nikkhah, M.; Akbari, M.; Paul, A.; Memic, A.; Dolatshahi-Pirouz, A.; Khademhosseini, A., Gelatin-Based Biomaterials For Tissue Engineering And Stem Cell Bioengineering. *Biomaterials from Nature for Advanced Devices and Therapies* **2016**, 37-62, DOI: 10.1002/9781119126218.ch3

56. Fairbanks, B. D.; Macdougall, L. J.; Mavila, S.; Sinha, J.; Kirkpatrick, B. E.; Anseth, K. S.; Bowman, C. N., Photoclick Chemistry: A Bright Idea. *Chemical Reviews* **2021,** *121* (12), 6915-6990, DOI: 10.1021/acs.chemrev.0c01212

57. Hoyle, C. E.; Bowman, C. N., Thiol–Ene Click Chemistry. *Angewandte Chemie International Edition* **2010,** *49* (9), 1540-1573, DOI: 10.1002/anie.200903924

58. McCall, J. D.; Anseth, K. S., Thiol–Ene Photopolymerizations Provide a Facile Method To Encapsulate Proteins and Maintain Their Bioactivity. *Biomacromolecules* **2012,** *13* (8), 2410-2417, DOI: 10.1021/bm300671s

59. Van Hoorick, J.; Gruber, P.; Markovic, M.; Rollot, M.; Graulus, G.-J.; Vagenende, M.; Tromayer, M.; Van Erps, J.; Thienpont, H.; Martins, J. C.; Baudis, S.; Ovsianikov, A.; Dubruel, P.; Van Vlierberghe, S., Highly Reactive Thiol-Norbornene Photo-Click Hydrogels: Toward Improved Processability. *Macromolecular Rapid Communications* **2018,** *39* (14), 1800181, DOI: 10.1002/marc.201800181

60. Monteiro, N.; Thrivikraman, G.; Athirasala, A.; Tahayeri, A.; França, C. M.; Ferracane, J. L.; Bertassoni, L. E., Photopolymerization of cell-laden gelatin methacryloyl hydrogels using a dental curing light for regenerative dentistry. *Dental Materials* **2018,** *34* (3), 389-399, DOI: 10.1016/j.dental.2017.11.020

61. Benedikt, S.; Wang, J.; Markovic, M.; Moszner, N.; Dietliker, K.; Ovsianikov, A.; Grützmacher, H.; Liska, R., Highly efficient water-soluble visible light photoinitiators. *Journal of Polymer Science Part A: Polymer Chemistry* **2016,** *54* (4), 473-479, DOI: 10.1002/pola.27903

62. Murphy, C. M.; Haugh, M. G.; O'Brien, F. J., The effect of mean pore size on cell attachment, proliferation and migration in collagen–glycosaminoglycan scaffolds for bone tissue engineering. *Biomaterials* **2010,** *31* (3), 461-466, DOI: 10.1016/j.biomaterials.2009.09.063

63. Loh, Q. L.; Choong, C., Three-Dimensional Scaffolds for Tissue Engineering Applications: Role of Porosity and Pore Size. *Tissue Engineering Part B: Reviews* **2013,** *19* (6), 485-502, DOI: 10.1089/ten.teb.2012.0437

64. Qu, F.; Holloway, J. L.; Esterhai, J. L.; Burdick, J. A.; Mauck, R. L., Programmed biomolecule delivery to enable and direct cell migration for connective tissue repair. *Nature Communications* **2017,** *8* (1), 1780, DOI: 10.1038/s41467-017-01955-w

65. Lozinsky, V. I., Polymeric cryogels as a new family of macroporous and supermacroporous materials for biotechnological purposes. *Russian Chemical Bulletin* **2008,** *57* (5), 1015-1032, DOI: 10.1007/s11172-008-0131-7

66. Sahiner, N., Super macroporous poly(N-isopropyl acrylamide) cryogel for separation purpose. *Polymers for Advanced Technologies* **2018,** *29* (8), 2184-2191, DOI: 10.1002/pat.4326

67. Dainiak, M. B.; Galaev, I. Y.; Kumar, A.; Plieva, F. M.; Mattiasson, B., Chromatography of Living Cells Using Supermacroporous Hydrogels, Cryogels. In *Cell Separation: Fundamentals, Analytical and Preparative Methods*, Kumar, A.; Galaev, I. Y.; Mattiasson, B., Eds. Springer Berlin Heidelberg: Berlin, Heidelberg, 2007; pp 101-127, DOI: 10.1007/10_2006_044

68. Gyarmati, B.; Mészár, E. Z.; Kiss, L.; Deli, M. A.; László, K.; Szilágyi, A., Supermacroporous chemically cross-linked poly(aspartic acid) hydrogels. *Acta Biomaterialia* **2015,** *22*, 32-38, DOI: 10.1016/j.actbio.2015.04.033

69. Karvinen, J.; Ihalainen, T. O.; Calejo, M. T.; Jönkkäri, I.; Kellomäki, M., Characterization of the microstructure of hydrazone crosslinked polysaccharide-based hydrogels

through rheological and diffusion studies. *Materials Science and Engineering: C* **2019,** *94*, 1056-1066, DOI: 10.1016/j.msec.2018.10.048

70. Nicol, E., Photopolymerized Porous Hydrogels. *Biomacromolecules* **2021,** *22* (4), 1325-1345, DOI: 10.1021/acs.biomac.0c01671

71. Leal-Egaña, A.; Braumann, U.-D.; Díaz-Cuenca, A.; Nowicki, M.; Bader, A., Determination of pore size distribution at the cell-hydrogel interface. *Journal of Nanobiotechnology* **2011,** *9* (1), 24, DOI: 10.1186/1477-3155-9-24

72. Cuccia, N. L.; Pothineni, S.; Wu, B.; Méndez Harper, J.; Burton, J. C., Pore-size dependence and slow relaxation of hydrogel friction on smooth surfaces. *Proceedings of the National Academy of Sciences* **2020,** *117* (21), 11247-11256, DOI: 10.1073/pnas.1922364117

73. Jain, R. K.; Au, P.; Tam, J.; Duda, D. G.; Fukumura, D., Engineering vascularized tissue. *Nature Biotechnology* **2005,** *23* (7), 821-823, DOI: 10.1038/nbt0705-821

74. Richardson, S., On the no-slip boundary condition. *Journal of Fluid Mechanics* **1973,** *59* (4), 707-719, DOI: 10.1017/S0022112073001801

75. Blaeser, A.; Duarte Campos, D. F.; Puster, U.; Richtering, W.; Stevens, M. M.; Fischer, H., Controlling Shear Stress in 3D Bioprinting is a Key Factor to Balance Printing Resolution and Stem Cell Integrity. *Advanced Healthcare Materials* **2016,** *5* (3), 326-333, DOI: 10.1002/adhm.201500677

76. Cidonio, G.; Glinka, M.; Dawson, J. I.; Oreffo, R. O. C., The cell in the ink: Improving biofabrication by printing stem cells for skeletal regenerative medicine. *Biomaterials* **2019,** *209*, 10-24, DOI: 10.1016/j.biomaterials.2019.04.009

77. Bae, Y. B.; Jang, H. K.; Shin, T. H.; Phukan, G.; Tran, T. T.; Lee, G.; Hwang, W. R.; Kim, J. M., Microfluidic assessment of mechanical cell damage by extensional stress. *Lab on a Chip* **2016,** *16* (1), 96-103, DOI: 10.1039/C5LC01006C

78. Tanzeglock, T.; Soos, M.; Stephanopoulos, G.; Morbidelli, M., Induction of mammalian cell death by simple shear and extensional flows. *Biotechnology and Bioengineering* **2009,** *104* (2), 360-370, DOI: 10.1002/bit.22405

79. Costantini, M.; Testa, S.; Fornetti, E.; Barbetta, A.; Trombetta, M.; Cannata, S. M.; Gargioli, C.; Rainer, A., Engineering Muscle Networks in 3D Gelatin Methacryloyl Hydrogels: Influence of Mechanical Stiffness and Geometrical Confinement. *Frontiers in Bioengineering and Biotechnology* **2017,** *5*, DOI: 10.3389/fbioe.2017.00022

80. Zhuang, P.; An, J.; Chua, C. K.; Tan, L. P., Bioprinting of 3D in vitro skeletal muscle models: A review. *Materials & Design* **2020,** *193*, 108794, DOI: 10.1016/j.matdes.2020.108794

81. Khodabukus, A.; Prabhu, N.; Wang, J.; Bursac, N., In Vitro Tissue-Engineered Skeletal Muscle Models for Studying Muscle Physiology and Disease. *Advanced Healthcare Materials* **2018,** *7* (15), 1701498, DOI: 10.1002/adhm.201701498

82. Cittadella Vigodarzere, G.; Mantero, S., Skeletal muscle tissue engineering: strategies for volumetric constructs. *Frontiers in Physiology* **2014,** *5*, DOI: 10.3389/fphys.2014.00362

83. Samandari, M.; Quint, J.; Rodríguez-delaRosa, A.; Sinha, I.; Pourquié, O.; Tamayol, A., Bioinks and Bioprinting Strategies for Skeletal Muscle Tissue Engineering. *Advanced Materials* **2021,** *n/a* (n/a), 2105883, DOI: 10.1002/adma.202105883

84. Schäfer, B.; Cai, A.; Ruhl, T.; Beier, J. P., Chapter 14 - Skeletal muscle tissue engineering. In *Tissue Engineering Using Ceramics and Polymers (Third Edition)*, Boccaccini, A. R.; Ma, P. X.; Liverani, L., Eds. Woodhead Publishing: 2022; pp 519-553, DOI: 10.1016/B978-0-12-820508-2.00015-5

85. Carnes, M. E.; Pins, G. D., Skeletal Muscle Tissue Engineering: Biomaterials-Based Strategies for the Treatment of Volumetric Muscle Loss. *Bioengineering* **2020,** *7* (3) , DOI: 10.3390/bioengineering7030085

86. Gilbert-Honick, J.; Grayson, W., Vascularized and Innervated Skeletal Muscle Tissue Engineering. *Advanced Healthcare Materials* **2020,** *9* (1), 1900626, DOI: 10.1002/adhm.201900626

87. Naranjo, J. D.; Dziki, J. L.; Badylak, S. F., Regenerative Medicine Approaches for Age-Related Muscle Loss and Sarcopenia: A Mini-Review. *Gerontology* **2017,** *63* (6), 580-589, DOI: 10.1159/000479278

88. Cai, Z.; Liu, D.; Yang, Y.; Xie, W.; He, M.; Yu, D.; Wu, Y.; Wang, X.; Xiao, W.; Li, Y., The role and therapeutic potential of stem cells in skeletal muscle in sarcopenia. *Stem Cell Research & Therapy* **2022,** *13* (1), 28, DOI: 10.1186/s13287-022-02706-5

89. Wang, P.-Y.; Yu, H.-T.; Tsai, W.-B., Modulation of alignment and differentiation of skeletal myoblasts by submicron ridges/grooves surface structure. *Biotechnology and Bioengineering* **2010,** *106* (2), 285-294, DOI: 10.1002/bit.22697

90. Liao, I. C.; Liu, J. B.; Bursac, N.; Leong, K. W., Effect of Electromechanical Stimulation on the Maturation of Myotubes on Aligned Electrospun Fibers. *Cellular and Molecular Bioengineering* **2008,** *1* (2), 133-145, DOI: 10.1007/s12195-008-0021-y

91. Azevedo, M.; Baylies, M. K., Getting into Position: Nuclear Movement in Muscle Cells. *Trends in Cell Biology* **2020,** *30* (4), 303-316, DOI: 10.1016/j.tcb.2020.01.002

92. Rozwadowska, N.; Kolanowski, T.; Wiland, E.; Siatkowski, M.; Pawlak, P.; Malcher, A.; Mietkiewski, T.; Olszewska, M.; Kurpisz, M., Characterisation of Nuclear Architectural Alterations during In Vitro Differentiation of Human Stem Cells of Myogenic Origin. *PLOS ONE* **2013,** *8* (9), e73231, DOI: 10.1371/journal.pone.0073231

93. Roman, W.; Gomes, E. R., Nuclear positioning in skeletal muscle. *Seminars in Cell & Developmental Biology* **2018,** *82*, 51-56, DOI: 10.1016/j.semcdb.2017.11.005

94. Espigat-Georger, A.; Dyachuk, V.; Chemin, C.; Emorine, L.; Merdes, A., Nuclear alignment in myotubes requires centrosome proteins recruited by nesprin-1. *Journal of Cell Science* **2016,** *129* (22), 4227-4237, DOI: 10.1242/jcs.191767

For Table of Contents Only

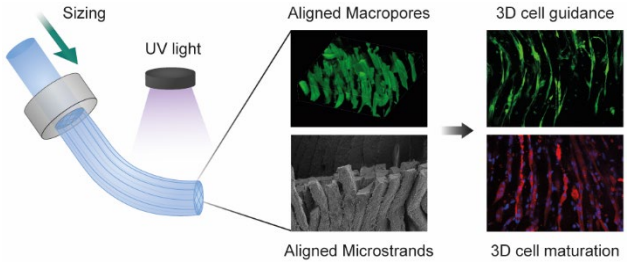
Sizing
UV light
Aligned Macropores
3D cell guidance
Aligned Microstrands
3D cell maturation